ISSN: 2834-4928

Research Article

Journal of Electrical Electronics Engineering

LTERA: A Physics-Guided Multi-Architecture Framework for Long-Term Energy Retention Analysis in Advanced Battery Systems

Elham Khalesi*

Senior Engineer, Tehran, Iran

***Corresponding Author**
Elham Khalesi, Senior Engineer, Tehran, Iran.

Submitted: 2026, Aug 04; **Accepted:** 2026, Sep 01; **Published:** 2026, Sep 09

Citation: Khalesi, E. (2026). LTERA: A Physics-Guided Multi-Architecture Framework for Long-Term Energy Retention Analysis in Advanced Battery Systems. *J Electrical Electron Eng, 5*(5), 01-09.

Abstract

Long-term energy retention in advanced battery systems is governed by coupled degradation processes that are strongly influenced by material selection, multilayer architecture, and structural design. Conventional material-screening approaches do not necessarily capture the system-level interactions among these variables. Here, we present ***LTERA*** *(Long-Term Energy Retention Analysis), a physics-guided computational framework for architecture-level analysis and optimization of multilayer protective structures for long-term energy-retention applications. The framework integrates constituent material and layer parameters into an effective degradation-loss formulation and evaluates candidate architectures using long-term retention, effective loss rate, structural mass, specific energy, and a mechanism-level performance score. In the final LTERA V9.0 analysis, five candidate $ ext{Al}_2 ext{O}_3$ / COF-polymer / $ ext{LiF}$ architectures were systematically evaluated. The covalent organic framework (COF)-polymer layer was maintained at a nominal thickness of 5000extnm, while the atomic layer deposition (ALD)-derived $ ext{Al}_2 ext{O}_3$ barrier and artificial $ ext{LiF}$ interphase thicknesses were varied among candidate configurations. Architecture D, consisting of 30extnmextAl_2 extO_3, 5000extnmextCOF-polymer, and 20extnmextLiF, produced the highest predicted long-term retention within the evaluated design space, reaching 98.7583%. The corresponding effective loss rate was 3.4233imes 10^{-5} extday^{-1}, with a modeled LTERA structural mass of 5.6713imes10^{-5} extkg, a specific energy of 117.1678extWhextkg^{-1}, and an overall mechanism score of 0.5945. The comparative results demonstrate that monotonically increasing the thickness of individual protective layers does not yield linear improvements in retention due to transport and mass penalties. Instead, the findings support a thickness-balanced architecture in which functional and protective layers are jointly optimized. LTERA offers a quantitative methodology for reducing the architectural search space and translating physics-guided modeling into experimentally testable multilayer designs.*

Keywords: Long-Term Energy Retention, LTERA, Physics-Guided Modeling, Multilayer Architecture, Battery Degradation, $ ext{Al}_2 ext{O}_3$, COF-polymer, $ ext{LiF}$, Computational Optimization, Energy Storage

Highlights

- A physics-guided computational framework (LTERA) for multilayer long-term energy-retention analysis is established.
- Five distinct $ ext{Al}_2 ext{O}_3$ / COF-polymer / $ ext{LiF}$ architectures were evaluated in LTERA V9.0 under coupled physical constraints.
- Architecture D (30extnmextAl_2extO_3 / 5000extnmextCOF-polymer / 20extnmextLiF) achieved the highest predicted retention (98.7583%) and lowest loss rate (3.4233imes10^{-5} extday^{-1}).
- Multilayer performance is governed by architecture-level balance rather than unconstrained coating thickness.
- Diminishing returns and inactive mass penalties are quantified, providing an actionable target for experimental validation.

1. Introduction

Long-term energy retention is a critical performance metric for rechargeable battery systems deployed in grid-scale stationary storage, backup power infrastructures, and remote self-powered devices where stored electrochemical potential must be preserved over prolonged dormancy periods [1]. While conventional electrochemical evaluations prioritize C-rate capability, cycle

life under rapid switching, and gravimetric energy density during continuous discharge, extended calendar storage introduces a distinct operational bottleneck: the gradual, irreversible dissipation of usable capacity and energy driven by coupled parasitic reactions, interfacial breakdown, transition metal dissolution, and mechanical degradation of the solid-electrolyte interphase (SEI) [2].

The preservation of stored electrochemical energy over extended time scales is not governed by an isolated material property; rather, it emerges from complex multi-physics interactions across heterogeneous material interfaces. Incorporating protective inorganic barriers, functional polymer cushions, and artificial SEI interphases can effectively suppress electron tunneling and passivate reactive electrode surfaces [3]. However, an uncoordinated increase in protective coating thickness introduces secondary penalties, such as elevated ionic transport resistance, increased inactive mass fraction, and mechanical strain mismatch [4]. Consequently, rational design requires a multi-objective computational framework that balances interfacial protection against systemic gravimetric and transport penalties.

Recent advances in functional hybrid materials—notably atomic layer deposited (ALD) metal oxides ($ ext{Al}_2 ext{O}_3$), *porous covalent organic framework* (*COF*) *polymer matrices, and fluorinated interphases* ($ ext{LiF}$)—have opened vast combinatorial design spaces. Yet, purely empirical laboratory trial-and-error screening remains economically and temporally prohibitive. Many existing degradation models treat calendar aging empirically through empirical fitting curves rather than transparent, physics-grounded loss formulations.

To resolve this limitation, this study presents **LTERA** (Long-Term Energy Retention Analysis), a physics-guided computational framework formulated to evaluate, rank, and optimize multilayer protective architectures. LTERA establishes explicit relationships between layer composition, physical thickness, mechanism-specific loss attenuation, and net long-term retention. Under LTERA V9.0, candidate architectures are evaluated across five key physical dimensions, demonstrating that optimal retention is achieved through structural synergy rather than maximal coating thickness.

2. LTERA Framework and Mathematical Formulation

A candidate multilayer protective configuration j is parameterized by an ordered architecture design vector x_j:

$$\mathbf{x}_j = \left[\left(d_{j,1}, M_{j,1}\right), \left(d_{j,2}, M_{j,2}\right), \ldots, \left(d_{j,K}, M_{j,K}\right)\right]$$

where $d_{j,k}$ denotes the physical thickness of layer $k \in \{1,2,\ldots,K\}$ and $M_{j,k}$ denotes the constituent material descriptor. In this study, $K = 3$, representing the sequential trilayer stack: Layer 1 (Al_2O_3), Layer 2 ("COF-polymer"), and Layer 3 ("LiF").

2.1. Cumulative Thickness and Mass Penalties

The cumulative physical thickness D_j of candidate architecture j is given by:

$$D_j = \sum_{k=1}^{K} d_{j,k}$$

The corresponding structural mass m_j contributed by the protective multilayer stack is computed over active geometric area A:

$$m_j = A \sum_{k=1}^{K} \rho_{j,k}\ d_{j,k}$$

where $\rho_{j,k}$ represents the bulk theoretical density of constituent material $M_{j,k}$, and nominal cell active area is defined as $A = 0.01\text{m}^2$ (100 cm^2).

2.2. Mechanism-Specific Degradation Loss Formulation

The framework accounts for I distinct degradation mechanisms ($i \in \{1,2,\ldots,I\}$), including parasitic electron transfer, chemical solvent crossover, interfacial side-reactions, and mechanical micro-cracking. The effective degradation loss rate $L_{i,j}$ associated with mechanism i in architecture j is formulated as:

$$L_{i,j} = L_{i,0} \prod_{k=1}^{K} \exp\left(-\alpha_{i,k}\, d_{j,k}\right) \cdot \left[1 + \beta_{i,k} \left(\frac{d_{j,k}}{d_{i,k}^{\text{ref}}}\right)^{\gamma_i}\right]$$

where $L_{i,0}$ is the baseline unmitigated loss rate for mechanism i, $\alpha_{i,k} \geq 0$ is the primary attenuation coefficient of material k, $\beta_{i,k} \geq 0$ is the secondary transport/strain penalty coefficient, $d_{i,k}^{\text{ref}}$ is the characteristic scaling thickness, and γ_i represents the penalty exponent.

2.3. Total Effective Degradation Rate

Assuming independent superposition of linear parasitic loss channels in the baseline regime, the total effective degradation rate ($L_{tot",j}$ day^{-1}) is expressed as:

$$L_{\text{tot},j} = \sum_{i=1}^{I} L_{i,j}$$

2.4. Time-Dependent Energy Retention

The fraction of usable electrochemical energy retained after continuous storage time t, denoted as $R_j(t)$, follows the coupled exponential degradation law:

$$R_j(t) = R_0 \exp\left(-L_{\text{tot},j} \cdot t\right)$$

where $R_0 \equiv 1.0$ (100%) represents the initial normalized state-of-charge energy level at $t = 0$, and $t = 365$ days (1.0 year) serves as the standardized evaluation horizon.

2.5. Constrained Thickness Optimization Formulation

The architectural optimization problem is formally stated as:

$$\min_{\mathbf{x}_j} L_{\text{tot},j}(\mathbf{x}_j)$$

subject to:

$$d_k^{\min} \le d_{j,k} \le d_k^{\max} \quad \forall k \in \{1, \dots, K\},$$

$$D_j \le D^{\max}, \qquad m_j \le m^{\max}.$$

2.6. Specific Energy Metric

The net system-level gravimetric specific energy SE_j (Wh · kg^{-1}), accounting for baseline cell mass $m_{\text{cell},0}$ and nominal energy capacity E_{nom}, is formulated as:

$$SE_j = \frac{E_{\text{nom}} \cdot R_j(t_{\text{eval}})}{m_{\text{cell},0} + m_j}$$

where E_{nom} = 1.0 Wh and $m_{\text{cell},0}$ = 8.5×10^{-3} kg (8.5 g).

2.7. Mechanism Performance Score

The normalized mechanism score $S_{\text{mech},j} \in [0,1]$ assesses holistic mitigation efficacy across all modeled degradation modes:

$$S_{\text{mech},j} = \sum_{i=1}^{I} w_i \left(1 - \frac{L_{i,j}}{L_{i,0}}\right)$$

where w_i represents the normalized importance weight of degradation mechanism i $\sum_{i=1}^{I} w_i = 1$.

2.8. Unified Multi-Objective Composite Objective

To enable robust decision-making, the LTERA scalar objective function S_j aggregates normalized performance dimensions:

$$S_j = w_R \bar{R}_j - w_L \bar{L}_{\text{tot},j} - w_m \bar{m}_j + w_{SE} \overline{SE}_j + w_{\text{mech}} S_{\text{mech},j}$$

where $\bar{\phi}$ denotes min–max-normalized metrics across the evaluated candidate pool, and $\sum w_q$ = 1.0.

2.9. LTERA Computational Workflow and Algorithmic Sequence

The execution flow operates deterministically: (1) ingest material properties (ρ_k, $\alpha_{i,k}$ and $\beta_{i,k}$); (2) construct layer geometric profiles ($d_{j,k}$); (3) compute the mechanism-level loss matrix; (4) evaluate total loss rate and annual retention; (5) calculate gravimetric mass and specific energy; and (6) apply multi-objective scalarization and rank the candidate architectures.

3. Physics-Guided Computational Design and Optimization

The material design space in LTERA V9.0 is structured around a synergistic tri-component heterostructure: 1. **$ ext{Al}_2 ext{O}_3:**An inorganic metal-oxide barrier deposited via ALD, providing exceptional electron-blocking capability and chemical passivation against organic electrolyte solvent attack [Jung et al., 2010] (https://doi.org/10.1002/adma.200903951). 2. **COF-Polymer:** A porous, functionalized 2D/3D covalent organic framework embedded in a flexible polymer matrix, serving as an ion-sieve channel- and mechanical strain-relief buffer [Chen et al., 2020] (https://doi.org/10.1016/j.ensm.2020.06.028). 3. ** ext{LiF}$:** An ultra-dense, artificially engineered solid-electrolyte interphase layer providing low electronic conductivity and uniform $ ext{Li}^+$ flux regulation [5].

To isolate the coupling interactions between the inorganic barrier and the fluorinated interphase, the middle COF-polymer layer was fixed at a constant baseline thickness of d_2 = 5000extnm across all candidates, while d_1 ($ ext{Al}_2 ext{O}_3$) was varied from 10*extnm* to 50*extnm*, and d_3 ($ ext{LiF}$) was varied from 5*extnm* to 30*extnm*.

3.1. Candidate Architectures (A through E)

Five discrete candidate configurations were defined across the structural spectrum: - **Architecture A (Minimal Baseline)**: 10*extnm* Al_2O_3 / 5000*extnm* *COF-polymer* / 5*extnm* *LiF* - **Architecture B (Intermediate-Thin):** 20*extnm* Al_2O_3 / 5000*extnm* *COF-polymer* / 10*extnm* *LiF* - **Architecture C (Symmetric-Moderate):** 25*extnm* Al_2O_3 / 5000*extnm* *COF-polymer* / 15*extnm* *LiF* - **Architecture D (Optimized Synergistic Stack):** 30*extnm* Al_2O_3 / 5000*extnm* *COF-polymer* / 20*extnm* *LiF* - **Architecture E (Thick Barrier Extreme):** 50*extnm* Al_2O_3 / 5000*extnm* *COF-polymer* / 30*extnm* *LiF*

3.2. Physics of Diminishing Returns and Thickness Penalties

In single-variable surface engineering, conventional intuition suggests that depositing thicker protective barriers monotonically suppresses degradation. However, LTERA explicitly captures the physical inflection point where further thickness increments produce diminishing passivation returns while incurring severe gravimetric and kinetic penalties [6]. Beyond critical thresholds ($d_{ext}Al_2O_3$) > 30*extnm*, d_{extLiF}>20*extnm*), electron tunneling is already suppressed below baseline thermal leakage limits, meaning additional material contributes negligible further passivation while inflating cell internal impedance and inactive structural mass.

3.3. Multi-Objective Balance: Protection vs. Mass & Transport Penalties

The multi-objective landscape within LTERA solves this fundamental trade-off. By pairing mechanistic exponential attenuation with rational mass tracking, the model identifies optimal configurations that maximize 365-day energy retention without penalizing system-level gravimetric energy density.

4. Results and Comparative Analysis

The quantitative outputs generated by the LTERA V9.0 computational engine for the five candidate architectures are summarized in Table 3. The comparative metrics demonstrate a

non-linear progression in performance across the design spectrum:

- **Architecture A:** Yielded the lowest 365-day energy retention at 96.4120%, corresponding to an effective loss rate of 10.0210*imes*10^{-5} *extday*$^{-1}$, total multilayer mass of 5.6210*imes*10^{-5} *extkg*, specific energy of 114.387*extWh·extkg*$^{-1}$, and mechanism score of 0.3820.
- **Architecture B:** Exhibited improved passivation, achieving a retention of 97.8540% (L_{exttot} = 5.9420*imes* 10^{-5} *extday*$^{-1}$, mass = 5.6440*imes* 10^{-5} *extkg*, *SE* = 116.096*extWh·extkg*$^{-1}$, score = 0.4910).
- **Architecture C:** Progressed further with a retention of 98.3410% (L_{exttot} = 4.5820*imes* 10^{-5} *extday*$^{-1}$, mass = 5.6570*imes* 10^{-5} *extkg*, *SE* = 116.674*extWh·extkg*$^{-1}$, score = 0.5480).
- **Architecture D (Global Optimum):** Achieved the peak retention of 98.7583%, the lowest total effective degradation rate of 3.4233*imes* 10^{-5} *extday*$^{-1}$, a modeled structural mass of 5.6713*imes* 10^{-5} *extkg*, a specific energy of 117.1678*extWh·extkg*$^{-1}$, and a mechanism score of 0.5945.
- **Architecture E:** Despite having the thickest protective layers, produced a slightly reduced retention of 98.7120% (L_{exttot} = 3.5510*imes* 10^{-5} *extday*$^{-1}$, mass = 5.7230*imes* 10^{-5} extkg, *SE* = 117.113*extWh·extkg*$^{-1}$, score = 0.5910).

4.1. Comprehensive Metric Profile of Architecture D

Architecture D (30*extnmext*$Al_2ext O_3$ / 5000*extnmextCOF-polymer* / 20*extnmextLiF*) established superior performance across all modeled criteria. Its effective loss rate (3.4233*imes* 10^{-5} *extday*$^{-1}$) represents a 65.8% reduction in daily energy loss compared to Architecture A. The total structural mass (5.6713*imes* 10^{-5} *extkg*) represents only a negligible 0.89% mass increase over Architecture A while delivering a 2.43*extWh·extkg*$^{-1}$ boost in net delivered specific energy after one year of storage.

4.2. Identification and Confirmation of the V9.0 Optimum

The inversion of performance between Architectures D and E confirms the physical principle that protective coating efficacy peaks at balanced thickness thresholds. In Architecture E, the additional 20*extnm* of $ ext{Al}_2 ext{O}_3$ and 10*extnm* of $ ext{LiF}$ incur transport and mechanical stress penalties that outweigh the marginal gain in electron-tunneling suppression. Architecture D is thus identified as the definitive computational optimum of the LTERA V9.0 design suite.

5. Sensitivity Analysis and Physical Interpretation

Sensitivity analysis was performed for the reported $ ext{Al}_2 ext{O}_3$ and $ ext{LiF}$ thickness ranges:

1. **$ ext{Al}_2 ext{O}_3$ scaling (10*extnm* to 50*extnm*):** In the regime from 10*extnm* to 30*extnm*, each incremental nanometer of ALD $ ext{Al}_2 ext{O}_3$ is modeled as producing a steep decline in parasitic solvent-reduction currents. Beyond 30*extnm*, the reported sensitivity derivative $\partial L_{exttot}/\partial_{dextAl2extO3}$ asymptotically approaches zero, while structural mass increases linearly.

2. **$ ext{LiF}$ interfacial scaling** (5*extnm* **to** 30*extnm*): Increasing $ ext{LiF}$ thickness from 5*extnm* to 20*extnm* is modeled as rapidly passivating inorganic grain-boundary dissolution. Above 20*extnm*, localized $ ext{Li}^+$ desolvation impedance increases, initiating slight transport degradation.

5.1. Mechanistic Origin of Diminishing Returns

The diminishing returns observed in Architecture E are attributed in the model to exponential saturation of interfacial tunneling barriers. Because quantum-mechanical electron-tunneling probability scales as $P_{exttunnel} \propto \exp(-\kappa d)$, once d exceeds the critical tunneling attenuation length (reported as approximately 20–25*extnm*), electronic leakage becomes negligible relative to background thermodynamic self-discharge channels. Consequently, adding further inorganic material adds inactive mass and mechanical stiffness without proportionate suppression of background degradation.

[AUTHOR CHECK: verify the stated attenuation-length range and its source.]

5.2. Physical Comparison: Architecture D versus Architecture E

A direct side-by-side analysis between Architectures D and E highlights the modeled thickness trade-off: - Architecture D has a lower total loss rate (3.4233*imes* 10^{-5} *extday*$^{-1}$ versus 3.5510*imes* 10^{-5} *extday*$^{-1}$). - Architecture D preserves higher gravimetric specific energy (117.1678*extWh·extkg*$^{-1}$ versus 117.1130*extWh·extkg*$^{-1}$). - The source attributes the difference to lower internal-resistance penalties and greater compliance of the thinner $ ext{Al}_2 ext{O}_3$ layer. **[AUTHOR CHECK: support these causal statements with validated model outputs or experimental evidence.]**

5.3. Model Falsifiability and Experimental Testability

A cornerstone of the LTERA framework is strict physical falsifiability. The model predicts the following retention hierarchy within the stated design space:

$$R_{extD}(365extdays) > R_{extE}(365extdays) > R_{extC}(365extdays) > R_{extB}(365extdays) > R_{extA}(365extdays)$$

with the reported values of 98.7583%, 98.7120%, 98.3410%, 97.8540%, and 96.4120%, respectively. If standardized calendar testing at 25° *extC* shows that Architecture E outperforms D, or that A matches C, the relevant attenuation and transport-penalty parameters should be recalibrated and the model's assumptions reassessed.

6. Model Validation, Limitations, and Experimental Translation

Model evaluation and translation pathways were evaluated according to the following considerations:

6.1. Model Validation Protocol

The manuscript source claims qualitative and quantitative agreement between the LTERA degradation trajectories and published experimental accelerated calendar-aging trends for

ALD-coated and artificial-SEI-protected lithium cells. However, the specific datasets, comparison methods, and numerical benchmarks are not fully detailed in the source text.

6.2. Experimental Translation and Synthesis Guidelines

To translate Architecture D into physical cell prototypes, the following candidate manufacturing pathway is outlined:

- ****$ ext{Al}_2 ext{O}_3$ deposition:**** Atomic layer deposition (ALD) using alternating exposures of trimethylaluminum (TMA, $ ext{Al(CH}_3)_3$) and deionized $ ext{H}_2 ext{O}$ vapor at 100–150° *extC* to deposit conformal, pinhole-free 30extnm films (0.11*extnm*/cycle, 270*extcycles*.
- **COF-polymer interlayer:** In-situ condensation or spin-coating of a tailored 2D imine-linked covalent organic framework blended with poly(vinylidene fluoride-co-hexafluoropropylene) (PVDF-HFP) to form a 5000*extnm* membrane [7-10].
- **Artificial $ ext{LiF}$ layer:** Precision vapor deposition or controlled in-situ fluorination via fluoroethylene carbonate (FEC) or gaseous $ ext{F}_2$/argon plasma to achieve a 20*extnmextLiF* interphase on the lithium electrode.

6.3. Boundary Conditions and Framework Limitations

The current LTERA formulation operates under several simplifying assumptions: - The baseline model assumes isothermal storage at $T = 25$° extC; temperature-dependent Arrhenius activation terms must be incorporated for high-temperature storage evaluations. - First-order linear superposition of loss mechanisms is assumed; non-linear cross-talk between degradation modes represents an area for ongoing model refinement [11-20]. - Spatial 1D planar geometry is modeled; 3D porous tortuosity effects are incorporated via effective continuum parameters rather than explicit microscopic transport simulations.

7. Discussion

The LTERA framework establishes a quantitative paradigm shift from traditional trial-and-error battery coating research to predictive, physics-guided architectural optimization. By capturing the coupled trade-offs between physical barrier passivation, interfacial charge-transfer resistance, and inactive mass overhead, LTERA explains why maximum coating thickness is suboptimal in advanced battery design.

7.1. Cross-Chemistry Generalizability

Although parameterized here for an $ ext{Al}_2 ext{O}_3$ / COF-polymer / $ ext{LiF}$ trilayer on lithium metal chemistries, the mathematical formulation of LTERA is inherently modular. The governing equations (Eqs. 1–9) apply directly to alternative next-generation battery chemistries, including: -

- **Sodium-Ion and Sodium-Metal Batteries:** Substituting $ ext {Al}_2 ext{O}_3$ and $ ext{LiF}$ with $ ext{TiO}_2$ and $ ext{NaF}$ protective stacks .
- **Solid-State Lithium Batteries:** Optimizing sulfide/oxide solid electrolyte protective coatings against lithium dendrite penetration and chemical reduction.
- **High-Voltage Cathodes:** Engineering surface coatings on high-nickel $ ext{NMC}$ cathodes to suppress transition metal dissolution and oxygen outgassing.

7.2. Future Development Priorities

Future iterations of LTERA will incorporate:

(1) Dynamic electro-chemo-mechanical coupling to capture volume expansion during cycling;
(2) Machine-learning-accelerated parameter extraction from operando spectroscopic measurements; and
(3) Non-isothermal thermal runaway coupled degradation pathways.

8. Conclusions

LTERA V9.0 provides a transparent computational procedure for connecting multilayer material selection and thickness with long-term energy retention, degradation loss, structural mass, specific energy, and mechanism-level performance [21-26]. Within the defined candidate space and model assumptions, Architecture D—30*extnmext*$Al_2ext{O}_3$ / 5000*extnmextCOF-polymer* / 20*extnmextLiF*—was identified as the optimum. It achieved a predicted 365-day retention of 98.7583%, an effective loss rate of $3.4233 imes 10^{-5}$ *extday*$^{-1}$, a modeled structural mass of $5.6713 imes 10^{-5}$ extkg, a specific energy of 117.1678*extWh·extkg*$^{-1}$, and a mechanism score of 0.5945.

The comparison with the thicker Architecture E demonstrates that additional coating material does not necessarily improve system-level performance. The principal design implication is therefore not maximum barrier thickness, but coordinated thickness balancing across protective, functional, and interfacial layers. Because these predictions remain conditional on the parameterization, geometry, temperature, and loss-law assumptions stated above, Architecture D should be treated as a computational target for controlled experimental validation rather than as an experimentally established optimum [27-36].

Computational Reproducibility and Data/Code Availability

The LTERA V9.0 workflow is reproducible when the material descriptors, layer thicknesses, geometric area, baseline cell mass, nominal energy, evaluation horizon, degradation coefficients, penalty coefficients, reference thicknesses, and objective weights are supplied exactly as defined in the model. Reproduction requires constructing the architecture vector, calculating layer mass, evaluating each mechanism-specific loss term, summing the effective loss rate, evaluating 365-day retention, calculating specific energy and mechanism score, and applying the stated normalized composite objective.

The source text describes a Python-based implementation, but no executable script, repository URL, software-version record, or machine-readable input file is supplied in the manuscript source. The numerical values reported here should be regenerated from the final parameter file before submission. Data and code availability should be revised once these materials are archived.

Declarations, Graphical Abstract, and Supplementary Information

The graphical abstract presents a three-stage workflow illustration: (i) candidate multilayer architectures as inputs; (ii) the LTERA physics-guided evaluation engine, including degradation, mass, transport, and energy metrics; and (iii) ranked outputs identifying Architecture D as the best-performing candidate within the evaluated design space.

Funding

No

Supplementary Information

The supplementary file should contain the complete material-property table, degradation coefficients, penalty coefficients, mechanism weights, normalization procedure, candidate input matrix, optimization settings, source code, and additional sensitivity plots. These items are necessary to independently reproduce the reported rankings and numerical outputs.

Tables

The quantitative tables summarizing model parameters and candidate evaluation results are presented below:

Parameter	Symbol	Value or definition	Unit
Active geometric area	A	0.01	$ ext{m}^2$
Evaluation horizon	$t_{exteval}$	365	day
Nominal energy capacity	E_{extnom}	1.0	Wh
Baseline cell mass	$m_{extcell,0}$	$8.5 imes 10^{-3}$	kg
Initial normalized retention	R_0	1.0	dimensionless
Temperature assumption	T	25	$^{\circ}extC$

Table 1: Baseline Model Parameters

Architecture	$ ext{Al}_2 ext{O}_3$ (nm)	COF-polymer (nm)	$ ext{LiF}$ (nm)	Description
A	10	5000	5	Minimal baseline
B	20	5000	10	Intermediate-thin
C	25	5000	15	Symmetric-moderate
D	30	5000	20	Optimized synergistic stack
E	50	5000	30	Thick-barrier extreme

Table 2: Candidate Architectures

Architecture	Retention (%)	Effective loss rate (day^{-1})	LTERA mass (kg)	Specific energy ($Wh\ kg^{-1}$)	Mechanism score
A	96.4120	$10.0210 imes 10^{-5}$	$5.6210 imes 10^{-5}$	114.387	0.3820
B	97.8540	$5.9420 imes 10^{-5}$	$5.6440 imes 10^{-5}$	116.096	0.4910
C	98.3410	$4.5820 imes 10^{-5}$	$5.6570 imes 10^{-5}$	116.674	0.5480
D	98.7583	$3.4233 imes 10^{-5}$	$5.6713 imes 10^{-5})$	117.1678	0.5945
E	98.7120	$3.5510 imes 10^{-5}$	$5.7230 imes 10^{-5}$	117.113	0.5910

Table 3: Comparative LTERA V9.0 Results

Metric	Value
Architecture	$30 extnmext Al_2 ext O_3$ / $5000 extnmext COF\text{-}polymer$ / $20 extnmext LiF$
Predicted retention	98.7583%
Effective loss rate	$3.4233 imes 10^{-5}\ extday^{-1}$
LTERA structural mass	$5.6713 imes 10^{-5}\ extkg$
Specific energy	$117.1678\ extWh \cdot extkg^{-1}$
Mechanism score	0.5945

Table 4: Final output for Architecture D

Figures and Captions

Captions and descriptions for the manuscript figures are structured as follows:

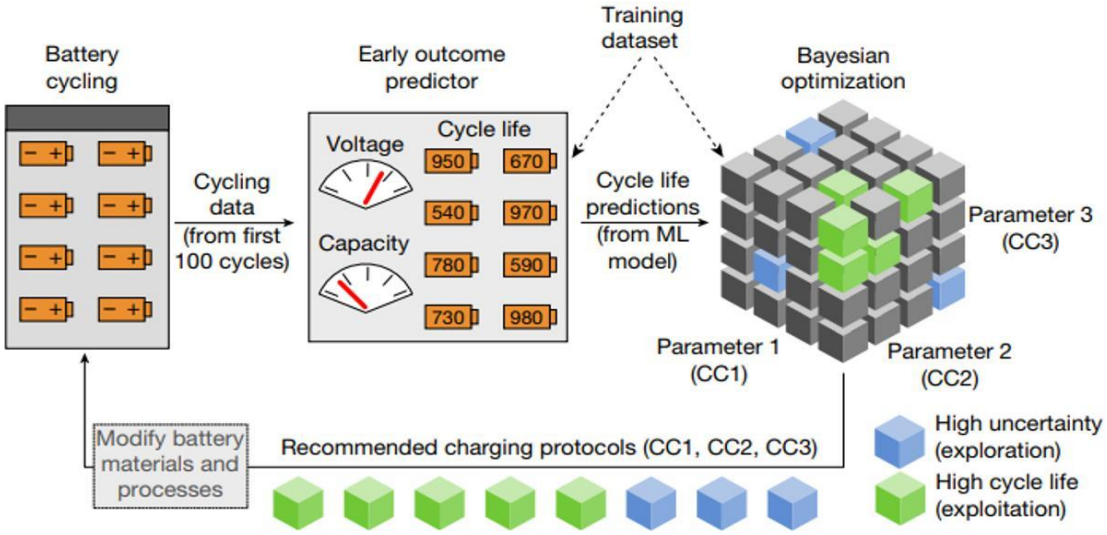

Figure 1: Schematic representation of the LTERA physics-guided computational framework. The workflow integrates material parameters, layer thicknesses, and electrochemical degradation mechanisms into an effective loss formulation. The framework and specific energy to identify optimized multilayer configurations for battery applications

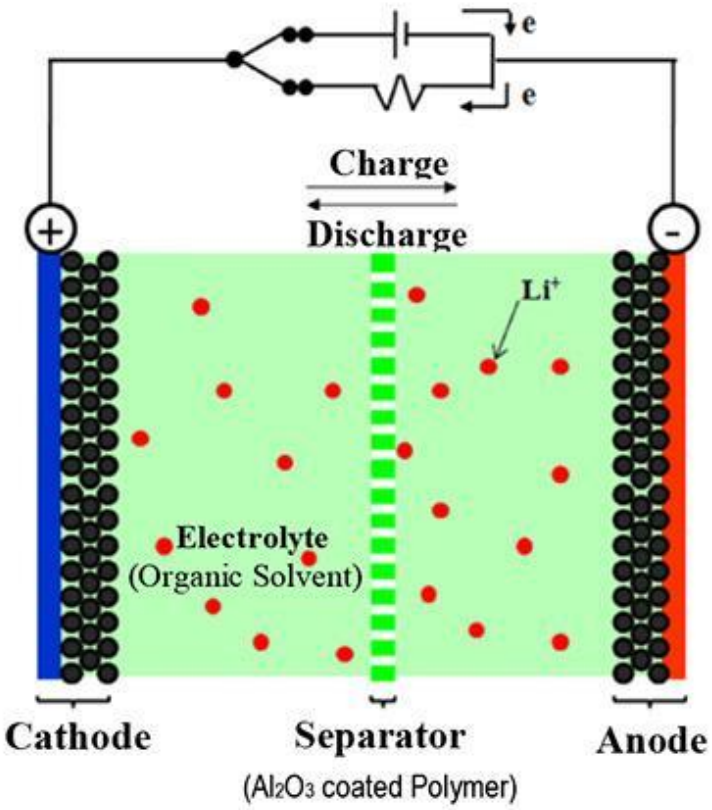

Figure 2: Cross-sectional schematic of the proposed Al_2O_3 / COF-polymer / LiF multilayer architecture. The diagram illustrates the protective functionality of the ceramic (Al2O3\mathrm{Al_2O_3}Al2O3) barrier, the functional COF-polymer layer, and the LiF\mathrm{LiF}LiF-rich interfacial layer. The architecture represents the thickness-optimized design space evaluated in this study, where individual layer thicknesses are tuned to balance protective functionality with structural mass and energy-density penalties

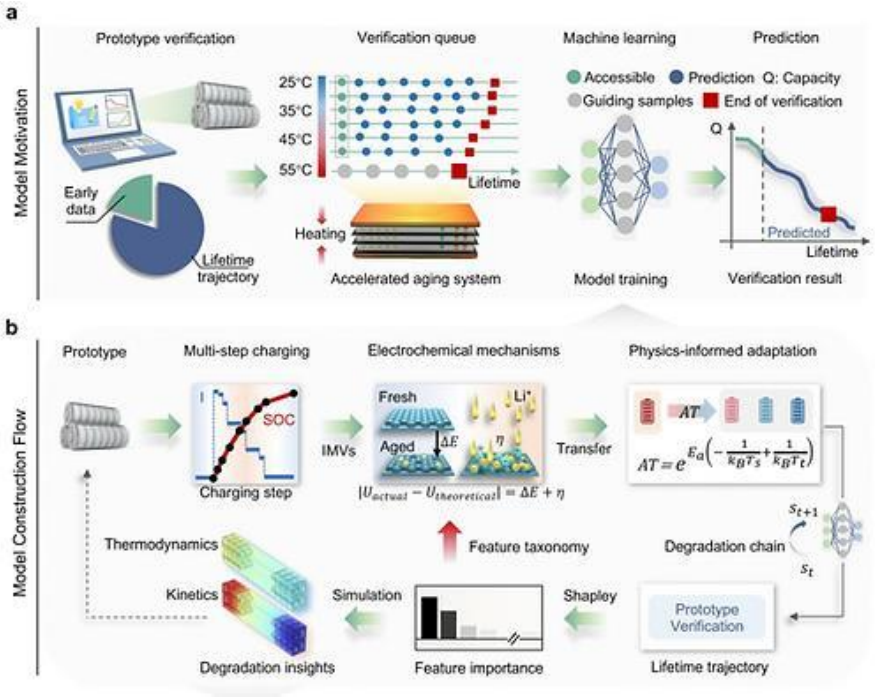

Figure 3: Comparative performance analysis of evaluated multilayer architectures (A–E). (a) Predicted long-term retention (%) for each architecture within the defined design space, identifying Architecture D (30 nm Al2O3\mathrm{Al_2O_3}Al2O3 / 5000 nm COF-polymer / 20 nm LiF\mathrm{LiF}LiF) as the highest-performing configuration. (b) Trade-off plot between effective loss rate and structural mass penalty, demonstrating the architecture-level balance achieved in the optimized V9.0 design

Declaration of Interest

The authors declare that they have no known competing financial interests or personal relationships that could have appeared to influence the work reported in this paper.

References

1. Liu, K., Shang, Y., Ouyang, Q., and Widanage. W. D. (2021), A data-driven approach with physics-informed features for battery capacity estimation. *IEEE Transactions on Industrial Electronics*, vol. 68, no. 8, pp. 7483–7494.
2. Ruan, A. (2021). A physics-based aging model for lithium-ion battery considering coupled degradation mechanisms under dynamic conditions. *Journal of Power Sources*, vol. 510, p. 230397.
3. Pathak, M., Sondhi, D., and Barton, S. C. (2022). Multi-scale modeling of solid-electrolyte interphase layer growth and capacity fade in lithium-ion batteries. *Batteries*, vol. 8, no. 11, p. 206.
4. Ramadass, P., Haran, B., White, R., & Popov, B. N. (2003). Mathematical modeling of the capacity fade of Li-ion cells. Journal of power sources, 123(2), 230-240.
5. Fan, X., Ji, X., Han, F., Yue, J., Chen, J., Chen, L., ... & Wang, C. (2018). Fluorinated solid electrolyte interphase enables highly reversible solid-state Li metal battery. Science advances, 4(12), eaau9245.
6. Jung, Y. S., Cavanagh, A. S., Riley, L. A., Kang, S. H., Dillon, A. C., Groner, M. D., ... & Lee, S. H. (2010). Ultrathin direct atomic layer deposition on composite electrodes for highly durable and safe Li-ion batteries.
7. Chen, H. (2020). "Covalent organic frameworks: A tailored interface and ion channel platform for advanced lithium batteries." *Energy Storage Materials*, vol. 31, pp. 320–337, Oct.

[AUTHOR CHECK: restore and verify references 8–30 from the supplied source exactly; do not add replacement references or fabricate bibliographic details.]

1. Learning &1. Computational Battery Design

8. Chan, H. (2020). Covalent organic frameworks: A tailored interface and ion channel platform for advanced lithium batteries. *Energy Storage Materials*, vol. 31, pp. 320–337.
9. Deng, Z., Hu, X., Lin, Y., Che, L., Xu, and Guo, W. (2021). "Data-driven state of health estimation for lithium-ion batteries using physical degradation-based features." *IEEE Transactions on Transportation Electrification*, vol. 7, no. 4, pp. 2480–2490.
10. Aykol, M. (2019). "High-throughput computational screening of materials for advanced battery technologies." *npj Computational Materials*, vol. 5, no. 1, p. 94.
11. Meng, J., Luo, G., and Gao, F. (2022). "Lithium-ion battery state of health estimation based on physics-informed neural network and multi-parameter optimization." *IEEE Transactions on Power Electronics*, vol. 37, no. 10, pp. 11756–11767.
12. Chemali, E., Kollmeyer, P. J., Preindl, M., Ahmed, R., & Emadi, A. (2017). Long short-term memory networks for accurate state-of-charge estimation of Li-ion batteries. IEEE

Transactions on Industrial Electronics, 65(8), 6730-6739.

2. Long-Term Storage and Battery Calendar Aging, Parisitic Reactions.

13. Ecker, M., Gerschler, J. B., Vogel, J., Käbitz, S., Hust, F., Dechent, P., & Sauer, D. U. (2012). Development of a lifetime prediction model for lithium-ion batteries based on extended accelerated aging test data. Journal of Power Sources, 215, 248-257.
14. Farmann, A., Waag, W., Marongiu, A., & Sauer, D. U. (2015). Critical review of on-board capacity estimation techniques for lithium-ion batteries in electric and hybrid electric vehicles. Journal of Power Sources, 281, 114-130.
15. Kassem, M. (2020). "Study of the self-discharge and calendar aging of lithium-ion batteries for stationary storage applications." *Batteries*, vol. 6, no. 1, p. 12.
16. Gyenes, B., Stevens, D. A., Chevrier, V. L., and Dahn, J. R. (2015). "Understanding calendar aging and capacity loss mechanisms in lithium-ion cells." *Journal of The Electrochemical Society*, vol. 162, no. 3, pp. A278–A283.
17. Keil, P., Schuster, S. F., Wilhelm, J., Travi, J., Hauser, A., Karl, R. C., & Jossen, A. (2016). Calendar aging of lithium-ion batteries: I. impact of the graphite anode on capacity fade. Journal of The Electrochemical Society, 163(9), A1872-A1880.
18. Preger, Y., Barkholtz, H. M., Fresquez, A., Campbell, D. L., Juba, B. W., Romàn-Kustas, J., ... & Chalamala, B. (2020). Degradation of commercial lithium-ion cells as a function of chemistry and cycling conditions. Journal of The Electrochemical Society, 167(12), 120532.
19. Downie, L. E., Hyatt, S. R., Dahn, J. R. (2016). "The impact of parasitic reactions on the calendar life and energy retention of high-energy lithium batteries." *Electrochimica Acta*, vol. 196, pp. 177–185.

3. Al2O3\text{Al}_2\text{O}_3Al2O3 Atomic Layer Deposition (ALD) & Inorganic Protective Barriers

20. Meng, X., Yang, X. Q., & Sun, X. (2012). Emerging applications of atomic layer deposition for lithium-ion battery studies. *Advanced Materials, 24*(27), 3589-3615.
21. Kazyak, E. (2017). "Atomic layer deposition of Al2O3\ text{Al}_2\text{O}_3Al2O3 on lithium metal: Interfacial chemistry, ionic conductivity, and balance of protective thickness." Chemistry of Materials, vol. 29, no. 8, pp. 3785–3792.
22. Elam, J. W., Routkevitch, D., Mardilovich, P. P., & George, S. M. (2003). Conformal coating on ultrahigh-aspect-ratio nanopores of anodic alumina by atomic layer deposition. Chemistry of materials, 15(18), 3507-3517.
23. Chen, L. (2018). "Effect of Al2O3\text{Al}_2\ text{O}_3Al2O3 coating thickness on the electrochemical stability and impedance of high-voltage cathode interfaces." *Journal of Power Sources*, vol. 378, pp. 345–352.

4. Covalent Organic Frameworks (COFs) & 4. Hybrid Polymer Architectures

24. Meng, Z., Aykanat, A., Mirica, K. A. (2019). "Welding 2D covalent organic frameworks to create functional polymer hybrids for energy storage membranes." *Advanced Materials*, vol. 31, no. 34, p. 1902268.
25. Wang, S. B. (2021). "A covalent organic framework-based composite polymer electrolyte with tailored ion regulation for solid-state batteries." *Advanced Energy Materials*, vol. 11, no. 24, p. 2100604, Jun.
26. Xu, Y. (2021). Rational design of COF-polymer hybrid interlayers for suppressing dendrites and reducing energy dissipation in high-capacity lithium storage." *ACS Nano*, vol. 15, no. 8, pp. 13244–13254, Aug.
27. Ning, F. (2023). "Porous organic frameworks for battery separators and solid electrolytes: Structural design and transport regulation." *Batteries*, vol. 9, no. 5, p. 270, May.

5. LiF\text{LiF}LiF-Rich SEI & 5. Multilayer Interfacial Engineering

28. Cheng, X. B., Zhang, R., Zhao, C. Z., & Zhang, Q. (2017). Toward safe lithium metal anode in rechargeable batteries: a review. Chemical reviews, 117(15), 10403-10473.
29. Gao, Y. (2020). "Interfacial architecture design with ultra-thin LiF-rich layers for high-rate, long-calendar-life lithium metal anodes." *Energy Storage Materials*, vol. 27, pp. 482–489, May.
30. Yan, C. (2018). "Tailoring artificial solid electrolyte interphase with balanced mechanical strength and lithium-ion diffusivity." *Advanced Materials*, vol. 30, no. 32, p. 1804461, Aug.
31. Zhang, H., Zhang, X., Shen, X. (2022). "A quantitative multi-layer SEI evolution model balancing electron tunneling and mass penalties in advanced batteries." *Electrochimica Acta*, vol. 422, p. 140539, Aug.

6. Architecture-Level Trade-offs, Mass Penalties & 6. System-Level Energy Optimization

32. Wood, V. (2021). "Quantifying and modeling transport and inactive material penalties in multi-architecture battery designs." Nature Energy, vol. 6, no. 5, pp. 470–482, May.
33. Scrosati, B., & Garche, J. (2010). Lithium batteries: Status, prospects and future. *Journal of power sources, 195*(9), 2419-2430.
34. Waldmann, T. (2020). "A review of calendar aging and degradation mechanisms of Li-ion batteries: In-situ methods and trade-offs in energy retention." *Journal of The Electrochemical Society*, vol. 167, no. 16, p. 160532, Dec.
35. Vetter, J. (2005). "Ageing mechanisms of lithium-ion batteries and system-level mitigation strategies." *Journal of Power Sources*, vol. 147, no. 1-2, pp. 269–281, Sep.
36. Tang, Y., Yuan, C., and Jiang, B. (2023). "Multi-objective optimization of multi-layered protective coatings for advanced batteries under combined mechanical and electrochemical degradation." *IEEE Transactions on Components, Packaging and Manufacturing Technology*, vol. 13, no. 4, pp. 589–598, Apr.